Simulations of microflows induced by rotation of spirals in microchannels

Mustafa Koz, Serhat Yesilyurt[*]

Mechatronics Program, Sabanci University, Istanbul, Turkey

ABSTRACT

In microflows where Reynolds number is much smaller than unity, screwing motion of spirals is an effective mechanism of actuation as proven by microorganisms which propel themselves with the rotation of their helical tails. The main focus of this study is to analyze the flow enabled by means of a rotating spiral inside a rectangular channel, and to identify effects of parameters that control the flow, namely, the frequency and amplitude of rotations and the axial span between the helical rounds, which is the wavelength. The time-dependent three-dimensional flow is modeled by Stokes equation subject to continuity in a time-dependent deforming domain due to the rotation of the spiral. Parametric results are compared with asymptotic results presented in literature to describe the flagellar motion of microorganisms.

Keywords: Microflows, microchannels, microswimmer, flagellar propulsion, swimming bacteria.

1. INTRODUCTION

Microfluidic actuators consist of mainly micropumps which have a wide range of applications including cooling of electronic components, medical diagnosis, and drug delivery, lab-on-a-chip devices used in biology and chemistry, and space exploration[1]. The large scale actuation principles that rely on inertial effects cannot be adopted at microscales, where viscous effects dominate. Purcell draws a striking analogy between the conditions of a tar filled pool and a droplet of water for swimming of a person and a microorganism respectively[2].

Typically, microactuators such as micropumps rely on mechanical displacement and electric fields to propel the working fluid. Albeit achieved reliably with electroosmotic pumps, maintenance of steady controllable microflows remains a challenge for microfluidic applications that are sensitive to electric fields. Biologically inspired actuation mechanisms such as flagellar propulsion of a microorganism by means of a rotating spiral may prove useful. Microorganisms such as bacteria use their helical flagella actuated by protein-based motors to render a screwing motion resulting in net propulsion reaching to tens of tail lengths per second. Pioneering works of Sir James Gray[3], Sir Geoffrey Taylor[4], and Sir James Lighthill[5] build a solid foundation for the bio-fluid mechanics research on the swimming mechanisms of microorganisms based on the resistive force theory[6] and the slender body theory[7]. In recent years, there has been an increasing attention towards biologically inspired microfluidic applications such as design of micropumps[8,9,10] and microswimming robots[11,12] for medical applications.

Here, we present simulation-based analysis of microflows that are induced by the rotation of a spiral placed in a microchannel. The topology of the design corresponds to a micropump actuated by a rotating sprial. Unlike viscous pumps such as gear pumps and helical groove screw pumps, the mechanism analyzed here is not a reciprocating displacement pump but one that converts the perpendicular in-plane motion (rotation in the *yz*-plane) into the flow in the axial direction (*x*-direction) as shown in figure 1. The analysis is based on the following assumptions: time-dependent three-dimensional flow in the channel is governed by continuity and Stokes equations in a time-dependent domain that evolves according to rotating spiral. Analysis results present effects of the wavelength, amplitude and angular velocity of the spiral on time-averaged flow rate and rate-of-work done on the fluid, and are compared against analytical results of Lighthill[5] and Behkam and Sitti[12].

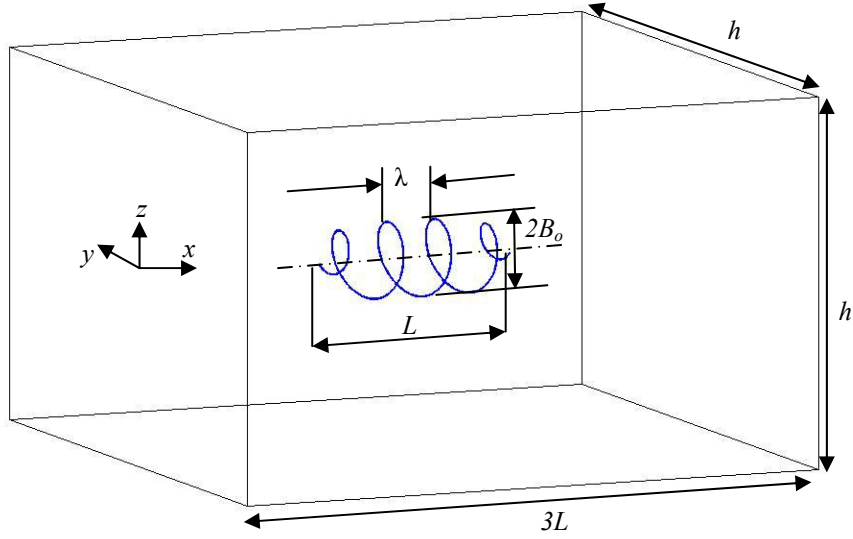[*] Corresponding author: syesilyurt@sabanciuniv.edu, +90(216)4839579.

Figure 1: Layout of the channel with a spiral placed inside as used in simulations.

2. METHODOLOGY

The model geometry is shown in figure 1. The rectangular channel has square cross-section of width and height, h, and length $3L$, where L is the axial length of the spiral. Rotation of the helical rod constitutes a three-dimensional traveling wave of length, λ, and amplitude, B_0 in the negative x-direction. The coordinate system is placed in the middle of the exit channel (left-side of the channel). The rotating motion of the spiral is prescribed as deformation of a rod in the yz-plane according to

$$\mathbf{d}_{rod}\left(x,t\right)=\begin{bmatrix} x_{rod} \\ y_{rod} \\ z_{rod} \end{bmatrix} = B\left(x\right)\begin{bmatrix} 0 \\ \sin\left(2\pi x/\lambda + \omega t\right) \\ \cos\left(2\pi x/\lambda + \omega t\right) \end{bmatrix} \quad . \tag{1}$$

In (1), $\omega = 2\pi f$ is the angular velocity of the rotations and f is the frequency, t is time, and $B(x)$ is the amplitude function which ensures the ends of the rod to be fixed, the helical deformation to have its maximum in the middle of the rod, and is given by:

$$B\left(x\right) = B_0\left(1 - \left[\frac{x-x_{mid}}{L/2}\right]^n\right). \tag{2}$$

In (2), B_0 is the maximum amplitude, n is a positive even integer that adjusts the distribution of the amplitude of the rotating wave, and x_{mid} is the x-coordinate of the midpoint of the rod.

The time-dependent, three-dimensional and incompressible flow in the microchannel is governed by unsteady Stokes equation in a deforming domain:

$$\rho\left(\frac{\partial \mathbf{U}}{\partial t} + \mathbf{u}_m \cdot \nabla \mathbf{U}\right) = -\nabla P + \mu \nabla^2 \mathbf{U} \;\; \text{in} \;\; \Omega\left(t\right), \tag{3}$$

subject to continuity,

$$\nabla \cdot \mathbf{U} = 0 \;\; \text{in} \;\; \Omega\left(t\right). \tag{4}$$

In equation (3), $\mathbf{U}$ is the velocity field of the flow, P is pressure, ρ is the density and μ is the viscosity of the fluid, and $\mathbf{u}_m$ is the velocity of the deforming domain with respect to initial domain, which corresponds to the channel with an undeformed straight rod of radius, r_0, placed in the middle. Thus, the $\mathbf{u}_m$ is defined by

$$\mathbf{u}_m\left(\mathbf{x}_{\Omega(t)},t\right) \equiv \left.\frac{d\mathbf{x}_{\Omega(t)}}{dt}\right|_{\Omega(0)} . \tag{5}$$

In effect, the velocity of the deforming domain is due to the Lagrangian definition of the flow, and corresponds to the moving mesh velocity in the finite-element representation[13].

Equations (3) and (4) are subject to no-slip boundary conditions on solid walls. Channel walls are stationary, thus the velocity is zero there. However, the rod deforms according to (1), and the velocity of this deformation is specified as

$$\mathbf{U}\left(\mathbf{x}_{rod},t\right) = \mathbf{v}_{rod}\left(x,t\right) = \begin{bmatrix} \dot{x}_{rod} \\ \dot{y}_{rod} \\ \dot{z}_{rod} \end{bmatrix} = \omega B\left(x\right) \begin{bmatrix} 0 \\ \cos\left(2\pi x/\lambda + \omega t\right) \\ -\sin\left(2\pi x/\lambda + \omega t\right) \end{bmatrix} . \tag{6}$$

In (6), $\mathbf{x}_{rod}$ is the coordinate vector of the surface of the rod, and is given by,

$$\mathbf{x}_{rod} = \mathbf{x}_0 + \mathbf{d}_{rod} , \tag{7}$$

where $\mathbf{x}_0$ is the surface of the undeformed rod of radius, r_0, and $\mathbf{d}_{rod}$ is given by (1).

Channel inlet and outlet pressures are set to zero:

$$\left[-P\mathbf{I}\right]\cdot\mathbf{n}\Big|_{x=0,y,z,t} = \left[-P\mathbf{I}\right]\cdot\mathbf{n}\Big|_{x=3L,y,z,t} = 0 , \tag{8}$$

where $\mathbf{n}$ is the outward normal of the surface.

The initial condition for (3) is the flow at rest, i.e. the velocity components are all equal to zero at $t = 0$:

$$\mathbf{U}(x,y,z,0) = \begin{bmatrix} 0 & 0 & 0 \end{bmatrix}^T . \tag{9}$$

To ensure the rest initial conditions, in numerical solutions an arbitrary ramp function is introduced as a factor on the moving boundary conditions on the rod during the first period of the rotation.

In order to compare the effects of parameters on the flow rate, first the time-dependent flow rate is calculated by integrating the velocity of the flow at the exit channel:

$$Q(t) = \int_{outlet} \mathbf{U}(x,y,z,t)\cdot\mathbf{n}\,dA . \tag{10}$$

Then the time- averaged flow rate is obtained by integrating $Q(t)$ over a period of time:

$$Q_{av} = \frac{1}{t_1-t_0}\int_{t_0}^{t_1} Q(t)\,dt . \tag{11}$$

Instantaneous rate of energy transferred to the fluid from the spiral, $\Pi(t)$, is computed by integrating the inner product of the y and z-components of the stress tensor with the velocity of the rotating helical rod, that is:

$$\Pi(t) = \int_{\substack{Rod \\ surface}} \Sigma\cdot\mathbf{v}_{rod}\,dA = \int_{\substack{Rod \\ surface}} \left[\Sigma_y\dot{y}_{rod} + \Sigma_z\dot{z}_{rod}\right]dA , \tag{12}$$

where Σ_y and Σ_z are y and z-components of the stress tensor, and are given by[13]:

$$\Sigma_y = \mu\left(\frac{\partial u}{\partial y} + \frac{\partial v}{\partial x}\right)n_x + \left(2\mu\frac{\partial v}{\partial y} - P\right)n_y + \mu\left(\frac{\partial v}{\partial z} + \frac{\partial w}{\partial y}\right)n_z, \tag{13}$$

and

$$\Sigma_z = \mu\left(\frac{\partial u}{\partial z} + \frac{\partial w}{\partial x}\right)n_x + \mu\left(\frac{\partial v}{\partial z} + \frac{\partial w}{\partial y}\right)n_y + \left(2\mu\frac{\partial w}{\partial z} - P\right)n_z. \tag{14}$$

In equations (13) and (14) n_x, n_y, and n_z are x, y and z components of the surface normal vector, The time-averaged power, Π_{av}, can be computed in a similar way to the time-averaged flow rate calculated in (11).

3. RESULTS

Numerical simulation results are obtained for dimensions and parameters of the spiral's motion that are presented in Table 1. In all cases, water is used as the working fluid. The reference case is for $f = 1$ Hz, $B_0 = 10$ μm, and $\lambda = 320$ μm.

Solutions to unsteady Stokes equation given by (3) subject to (4-8) are obtained using a commercial finite-element package COMSOL. In all simulations, quadratic Lagrange finite-elements (total of 12112) that generate 57662 degrees-of-freedom are used. Linear system of equations is solved with the parallel sparse direct solver, PARDISO, and the fifth degree interpolation polynomial in the backward-differentiation time-stepping method[13]. On average each simulation takes about 45 minutes on a double dual-core, 3.7GHz, Xeon processor workstation with 16 GB RAM, and running 64-bit SUSE 10.2 Linux operating system. Intel's level-3 BLAS libraries are used to invoke the automatic parallelization on two processors.

Quantity	Value
Channel width and height, h	200 μm
Channel length, $3L$	960 μm
Rod length, L	320 μm
Radius of the rod, r_0	10 μm
Viscosity of the fluid, μ	1.12×10^{-3} kg m^{-1}s^{-1}
Density of the fluid, ρ	10^3 kg m^{-3}
Frequency (reference case), $f*$	1 Hz
Amplitude (reference case), B_0*	10 μm
Wavelength (reference case), $\lambda*$	320 μm
Power in amplitude function, n	6

Table 1: The values of parameters used in the simulations.

In figure 2, normalized arrows display the flow velocity and color shading shows the pressure distribution at the bottom and side walls for the reference case at $t = 3$ sec. Pressure varies between -2.4 (dark blue) and 1.5 (dark red) mPa. Arrows representing the velocity vector are normalized to highlight the direction only. The flow is uniform at the inlet and exit of the channel, but near the rod, there is a strong recirculation due to the rotation of the spiral. At the middle of the spiral rod, rotating flow on the yz-plane is backwards near the bottom and forward near the top walls. The same bi-directional nature of the flow is observed near the fixed ends of the rod; however the rotation of flow diminishes at the ends. This behavior of the flow is also confirmed by the pressure distribution: flow is directed away from the high pressure and towards the low pressure regions.

In figure 3, the time-dependent flow rate, which is calculated by equation (11) for the reference case is shown. Despite the smoothness of the instantaneous snapshot shown in figure 2, area integration of the x-component of the velocity at the

exit ($x=0$) shows numerical noise due to its small magnitude. The average flow rate is 1.9×10^{-3} μl/min, which corresponds to the channel Reynolds number of 2.8×10^{-4}.
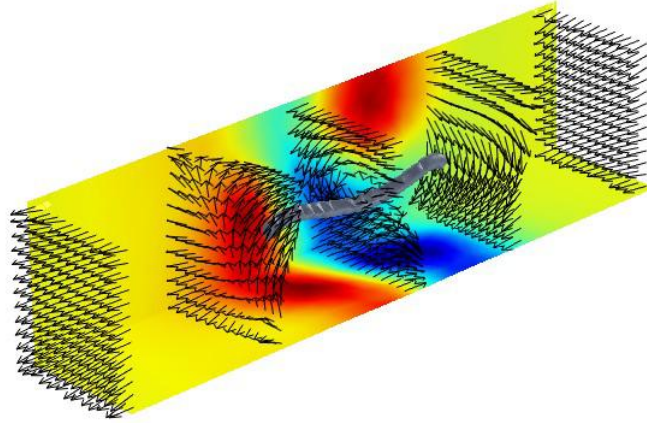

Figure 2: Velocity vectors and pressure distribution for the reference case (f = 1Hz, B_0 = 10 μm and λ = 320 μm) at t = 3 s; for clarity axes are removed.
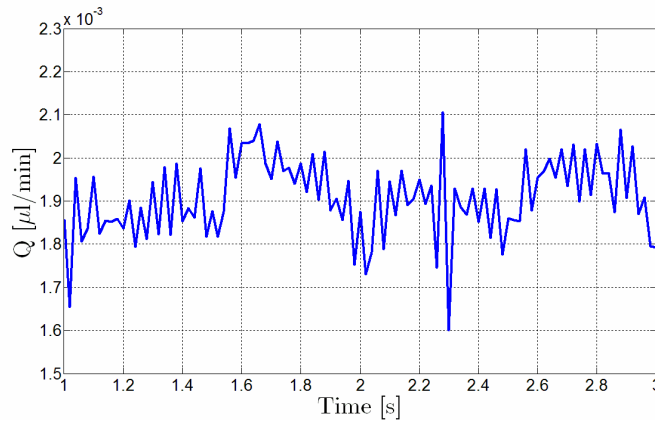
Figure 3: The channel flow rate for the reference case (f = 1Hz, B_0 = 10 μm and λ = 320 μm) as a function of time.

The variation of the time-averaged flow rate normalized by the reference case result with respect to frequency is shown in figure 4 along with the normalized velocity of a microswimmer having the same conditions. The base case velocity is 10.2536 μm/s. The plots of the normalized flow rate and the normalized velocity of the swimmer are nearly indiscernible, and indicate linear variation with the frequency. The velocity of the swimmer having the same conditions as helical rods in simulations is calculated by the expression developed by Behkam and Sitti[13] based on the resistive force theory[14]:

$$U = m\lambda V_\theta \sin\beta\cos\beta \frac{C_{n,helix} - C_{l,helix}}{n\lambda(C_{n,helix}\sin^2\beta + C_{l,helix} - C_{l,helix}\sin^2\beta) + 6\pi\mu a\cos\beta} \quad . \tag{15}$$

In (15), β is the angle between the helical rod and the plane of rotation, which is given by $\beta = \tan^{-1}(2\pi/\lambda B_0)$; $V_\theta = \omega B_0$ is the tangential velocity of the rotating spiral; $m = L/\lambda$ is the number of waves that reside on the rod; $C_{n,helix}$ and $C_{l,helix}$ are coefficients of resistance, which depend on λ, rod's radius, r_0, and fluid's viscosity, μ; and a is the radius of the head of the swimmer, which is zero here.
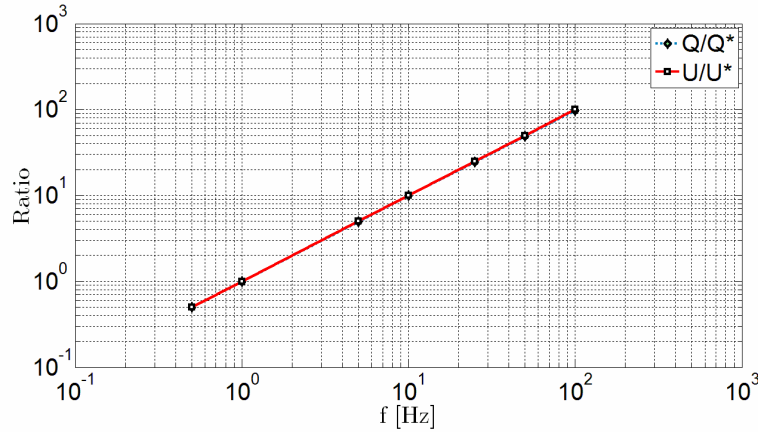
Figure 4: The effect of the frequency on the normalized flow rate and the normalized velocity of the swimmer with conditions: $f = 1$Hz, $B_0 = 10$ μm and $\lambda = 320$ μm.

In figure 5, the normalized flow rate and the normalized velocity of the swimmer having identical conditions with the simulations are plotted against the amplitude. The variation of the flow rate with the amplitude is quadratic. Simple theoretical results also indicate the same behavior for small amplitudes. Calculation of the velocity of the swimmer is based on inextensible flagella with finite-lengths, thus as the radius of the spiral's rotation increases (amplitude), the extent of the tail in the direction of helical axis shrinks. However, in our calculations we used a fixed extent of the spiral in the axial direction when comparing the performance of different rods. Thus, in effect, as the amplitude increases the spirals in our simulations have longer flagellar lengths, resulting in greater propulsion.
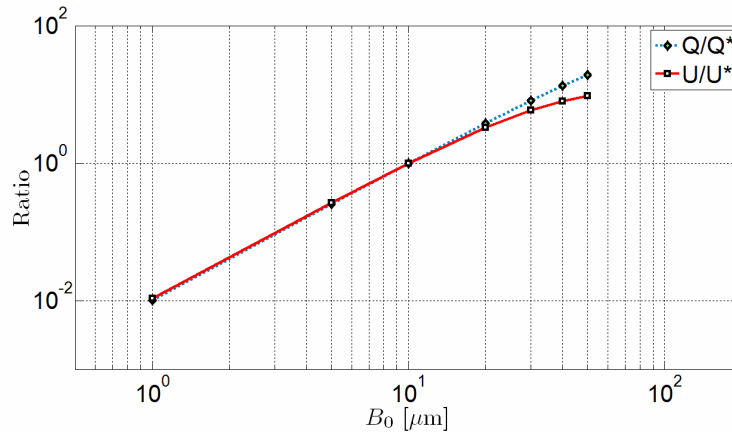

Figure 5: The effect of the amplitude on the normalized flow rate and the normalized velocity of the swimmer with conditions: $f = 1$Hz, $B_0 = 10$ μm and $\lambda = 320$ μm.

In figure 6, the effect of the wavelength on the flow rate is demonstrated, and compared with its effect on the velocity of a swimmer. The flow rate and the velocity of the swimmer are normalized with the results for the reference case parameters. Increasing wavelength results in decreasing flow rate as expected. One expects the velocity of the swimmer to converge to the wave-speed limit for small wavelengths without leaving improvement in the swimmer's velocity as the wavelength decreases further. However, the flow rate in the channel does not reach to that limit for the range of wavelengths used in simulations. Furthermore, the flow rate in the channel does not decrease with an increasing rate as the velocity of the swimmer does with increasing wavelength.

In figures 7 to 9, the rate of energy transfer from the spiral to the flow is plotted against the frequency, amplitude and wavelength respectively. The rate of energy transfer varies quadratically with the frequency. In the analysis presented by Lighthill[15], the rate of energy transfer is proportional to the square of the swimmer's velocity multiplied by a factor which is a complicated algebraic function of amplitude and wavelength, which is result of the assumption that the flagella are inextensible; in its short form:

$$\Pi_{av} \propto U^2 g\left(B_0, \lambda, L\right).$$ (16)

The quadratic dependence of the rate of energy transfer on the frequency agrees well with the Lighthill's prediction, as the flow rate (analogous to the velocity of the swimmer) varies linearly with the frequency as shown in figure 4, and predicted by a modified version of Lighthill's analysis[15] given by Behkam and Sitti[12] in equation (15).

According to figure 8, the effect of the amplitude on the rate of energy transfer is quadratic, which indicates that the function g in (16) has an inverse quadratic dependence on the amplitude when used for fixed length spirals.

Lastly, according to figure 9, the wavelength does not have much effect on the rate of energy transfer from the rod to the flow.
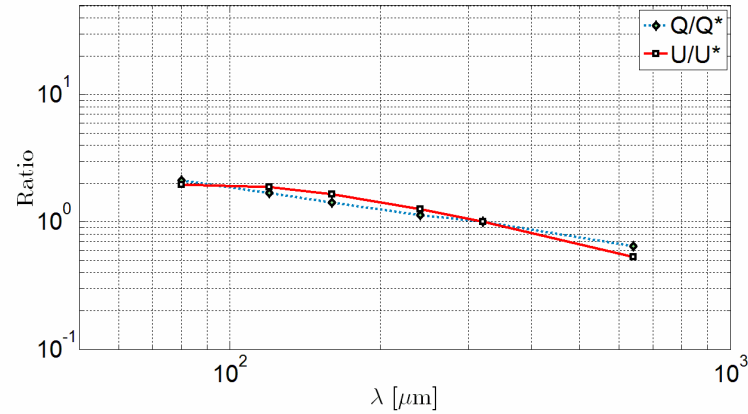

Figure 6: The effect of the wavelength on the normalized flow rate and the normalized velocity of the swimmer with identical conditions: $f = 1\text{Hz}$, $B_0 = 10$ μm and $\lambda = 320$ μm.
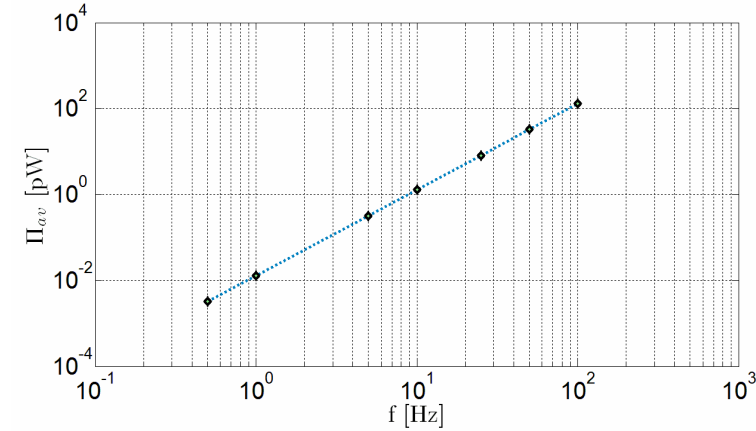

Figure 7: Time-averaged rate of energy transferred to the fluid as a function of frequency.

4. CONCLUSION

Simulations and analysis of microflows induced by rotating spirals in microchannels are presented here. Axial rotation of the spiral results in propagation of in-plane perpendicular waves in the direction of the axis of rotation. The screwing motion of the spiral, which is proven to be effective in propulsion of microorganisms, pushes the fluid inside a channel resulting in a net steady flow in the direction of the propagation. Simulations demonstrate that the instantaneous flow is steady at the channel inlet and exit planes, but flow rate varies in time. However, variations are not proven to be free from numerical noise. Overall the mechanism can be used viably in micropumps to render controllable steady flows.

Numerical-simulation experiments are carried out to find out effects of frequency, amplitude and wavelength on the time-averaged flow rate and the rate of energy transfer from the helical rod to the flow. Time-averaged flow rate in the channel is normalized with its value for the reference case and compared with the normalized velocity of a microswimmer that uses a helical tail that has the same parameters as ones used in simulations. The velocity of the swimmer is calculated from the formula presented by Behkam and Sitti[12], which is derived from the resistive force theory[7]. Time-averaged flow rate agrees well with its theoretical prediction. Agreement is superb for frequency and amplitude dependence at small amplitudes. For large amplitudes and wavelength dependence, differences between simulations and theory are observed. Differences are attributed to: in the theory, flagella are inextensible and have fixed lengths, but in simulations total length of spirals is kept constant allowing flagella to extend as amplitude and wavelength vary.

Lastly, according to simulation experiments the rate of energy transfer from the spiral to the flow varies quadratically with the frequency and amplitude, and remains unaffected by the wavelength. According to work presented by Lighthill[15] for swimming microorganisms, the quadratic frequency-dependence is due to square dependence of the energy transfer rate on the propulsion velocity which varies linearly by the frequency.
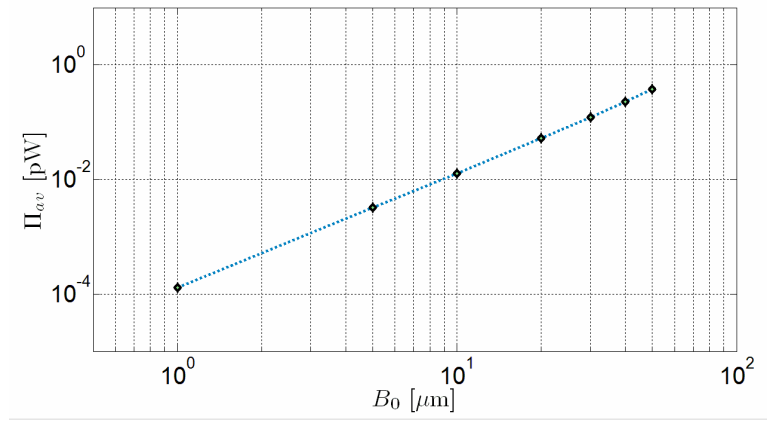

Figure 8: Time-averaged rate of energy transferred to the fluid as a function of amplitude.
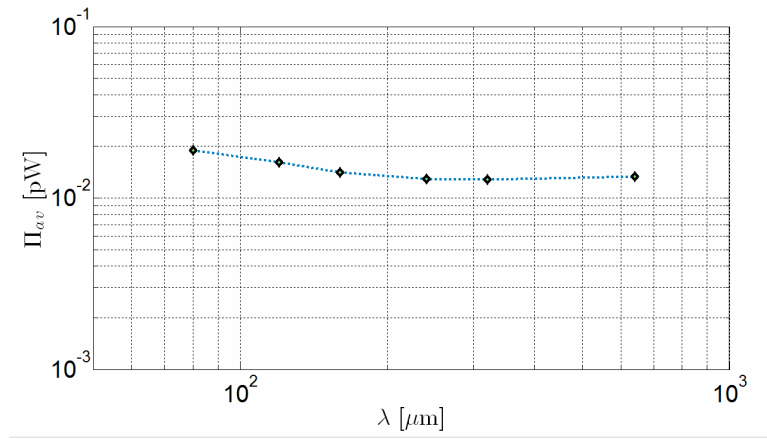

Figure 9: Time-averaged rate of energy transferred to the fluid as a function of wavelength.

ACKNOWLEDGMENTS

REFERENCES

1. D.J. Laser and J.G. Santiago, "A review of micropumps," *J. Micromech. Microeng*., **14**, R35-R64 (2004)
2. E.M. Purcell, "Life at Low Reynolds Number," *American Journal of Physics*, Vol. 45, No 1 (1977)
3. J. Gray, *Ciliary Movement*, Camb. Un. Press., Cambridge,1928.
4. Sir J. Lighthill, *Mathematical Biofluiddynamics*, Society for Industrial and Applied Mathematics, Philadelphia, 1975.
5. Sir G.I. Taylor, "Analysis of the Swimming of Microscopic Organisms," Proc Roy Soc*.,* A **209**, 447-61 (1951)
6. Sir G.I.Taylor, "Motion of axisymmetric bodies in viscous fluids," in Problems of Hydrodynamics and Continuum Mechanics, SIAM, 718-24 (1969)
7. J. Gray and G. J. Hancock, "Propulsion of Sea-Urchin Spermatozoa," J. Exp. Biol*.,* **32**, 802-814 (1955)
8. A.F. Tabak and S Yesilyurt, "Simulation-based analysis of flow due to traveling-plane-wave deformations on elastic thin-film actuators in micropumps," Microfluidcs and Nanofluidics, DOI:10.1007/s10404-007-0207y.
9. A.F. Tabak and S. Yesilyurt, "Numerical analysis of the 3D flow induced by propagationon of plane-wave deformations on thin membranes inside microchannels," Proceedings of the 5th International Conference on Nanochannels, Microchannels & Minichannels, ICNMM2007, Puebla, Mexico, (2007).
10. A.F. Tabak and S. Yesilyurt, "Numerical simulations and analysis of a micropump actuated by traveling plane waves," SPIE-Photonics West, MOEMS-MEMS, San Jose, (2007).
11. A.F. Tabak and S. Yesilyurt, "Numerical simulations of a traveling plane-wave actuator for microfluidic applications," ed. Jeri'Ann Hiller, Proceedings of the COMSOL Users Conference, Boston, (2006).
12. B. Behkam and M. Sitti, "Design methodology for biomimetic propulsion of miniature swimming robots," Journal of dynamic systems, measurement and control, **128**, 36-43, (2006).
13. COMSOL AB., *Comsol Multiphysics Modelling Guide,* 2007.
14. G.J. Hancock, "The self-propulsion of microscopic organisms through liquids," *Proceedings of the Royal Society of London Series A, Mathematical and Physical Sciences*, **217**, 96-121, The Royal Society, (1953).
15. Sir J. Lighthill, "Flagellar hydrodynamics: The von Neumann Lecture, 1975", *SIAM Review*, 18(2), 161-230 (1976)